Classification of chronic venous diseases based on skin temperature patterns

Dahlmanns, Stephan; Reich-Schupke, Stefanie; Schollemann, Franziska; Stücker, Markus; Leonhardt, Steffen; Teichmann, Daniel

Published in:
Physiological Measurement

DOI:
10.1088/1361-6579/abf020

Publication date:
2021

Document version:
Accepted manuscript

Physiological Measurement

Classification of chronic venous diseases based on skin temperature patterns

To cite this article before publication: Stephan Dahlmanns *et al* 2021 *Physiol. Meas.* in press https://doi.org/10.1088/1361-6579/abf020

Classification of chronic venous diseases based on skin temperature patterns

Stephan Dahlmanns[1], Stefanie Reich-Schupke[2], Franziska Schollemann[3], Markus Stücker[2], Steffen Leonhardt[1] and Daniel Teichmann[4,5]

[1] Chair for Medical Information Technology, Helmholtz Institute for Biomedical Engineering, RWTH Aachen University, Aachen 52074, Germany
[2] Department of Dermatology, Ruhr-University Bochum, Bochum 44791, Germany
[3] Department of Anesthesiology, Faculty of Medicine, RWTH Aachen University, Aachen 52074, Germany
[4] SDU Health Informatics and Technology, Maersk Mc-Kinney Moller Institute, University of Southern Denmark, Odense 5230, Denmark
[5] Institute for Medical Engineering and Science, Massachusetts Institute of Technology, Cambridge, MA, USA

E-mail: stephan.dahlmanns@rwth-aachen.de

Abstract. *Objective:* Infrared thermography has the potential to complement the classification of chronic venous diseases (CVD), but lacks sophisticated insights on the association between recorded skin temperatures and the severity of CVD. This research aims to identify temperature patterns in the lower legs of patients that are distinct in specific forms of CVD, including florid ulcers. *Methods:* Infrared images were acquired in a clinical trial with 36 patients and segmented using a region selection algorithm. The regions were analyzed with respect to seven predefined features. The most prominent thermal features were translated into rules to classify CVD. *Results:* Patients with mild forms of CVD show local increases in skin temperature by more than 1.5 °C. These regions were 2.0 °C warmer when CVD is more severe. Temperature variations of on average 0.4 °C occurred within venous leg ulcers. Furthermore, these wounds were 1.1 °C to 6.3 °C colder than periwound skin. *Conclusion:* Temperature patterns characterized by differences in temperature that occur within a few centimeters or millimeters are distinct to specific stages of CVD. These patterns are present in the locations of varicose veins and tissue damages. *Significance:* The findings increase the body of knowledge on the potential for the early detection of CVD using infrared thermography. Applying the presented algorithms and rules, infrared thermography may become a complementary tool for the objective classification of CVD.

Keywords: Infrared Thermography, Image Processing, Chronic Venous Diseases, Venous Leg Ulcer

Submitted to: *Physiol. Meas.*

1. Introduction

Chronic venous diseases (CVD) are a common age-related complication. The prevalence of chronic venous insufficiency (CVI), a severe form of CVD, is 17 % in Germany, with 0.1 % to 0.2 % of the population suffering from CVD-related chronic leg ulcers (Rabe et al. 2003, Heyer et al. 2016). Its treatment ranges from non-invasive approaches using compression stockings and venoactive drugs (Stücker et al. 2016) to the surgical removal of ulcers (Doerler et al. 2012). The treatment of one single ulcer approximately costs 10,000 euros per year (Purwins et al. 2010). It is therefore not surprising that current guidelines recommend to focus research on the early detection of factors that precede the progression of CVD to ulcers (National Institute for Health and Care Excellence 2013).

The different stages of CVD are described by the Clinical-Etiological-Anatomical-Pathophysiological (CEAP) classification (Eklöf et al. 2004). It categorizes CVD into seven clinical classes (C_0 to C_6). The subscript indicates the severity of the disease, C_3 or higher defining a CVI. No visible signs of a CVD result in C_0. Patients with spider or reticular varicose veins are classified as $C_1 - C_2$. Once edema occurs, CVI is apparent (C_3). Changes in skin tissue and healed ulcers belong to the classes C_4 and C_5, respectively. A CVI with florid ulcer is labeled as C_6. This visual and haptic classification is complemented by duplex sonography to detect varicose veins and to quantify the extend of truncal reflux (National Institute for Health and Care Excellence 2013). Findings suggest that the detection of this deep vein incompetence in combination with skin changes (C_4) best predicts ulceration (Robertson et al. 2009).

Whereas duplex sonography is an effective tool to assess harmful varicose veins, its application requires experienced professionals to detect these veins and to quantify their reflux. Furthermore, there exists a lack of evidence on the progression of varicose veins from $C_2 - C_3$ to the development of ulcers (C_6) (National Institute for Health and Care Excellence 2013). Furthermore, ulcer size measurements are usually performed only in the visible range using a meter measure or a RGB camera. For this reason, complementary approaches for the objective and automatic assessment of varicose veins and leg ulcers need to be investigated.

Infrared thermography may be such an approach, as wounds and the skin above varicose veins show different temperatures than healthy tissues (Bagavathiappan et al. 2008, Dini et al. 2015, Fierheller and Sibbald 2010, Gethin et al. 2018, Koerner et al. 2019, Martins et al. 2012, McGuiness et al. 2004, Sheffield et al. 1996, Trandel et al. 1975). These insights were gained by investigating discrete absolute temperature values within the wound or the skin surface. The aim of our research is to provide novel insights on the thermal properties of CVD, including ulcers. For this purpose, temperature patterns found in high resolution infrared images of the lower legs of patients with CVD were analyzed with the objective of assessing these patterns to the different stages of CVD.

2. Materials and Methods

The study methodology is summarized in figure 1. A total of 64 high resolution infrared images of the lower legs of patients with various degrees of CVD were recorded in a clinical trial. A region selection algorithm was applied to these images to detect potential regions of interest. These regions were then clustered into representative regions based on seven predefined features, each reflecting a specific thermal property. The resulting representative regions were analyzed to define threshold-based classification rules that assess every patient to one of four clinical classes of CVD. The thresholds of these rules were determined using sensitivity analysis respecting all regions to minimize the number of false positive classifications. The objective of this approach was to analyze different thermal properties in detail, rather than to compute algorithms that assess patients as quickly and robustly as possible. The computations were performed with the programming language MATLAB (The MathWorks, Natick, MA, USA).

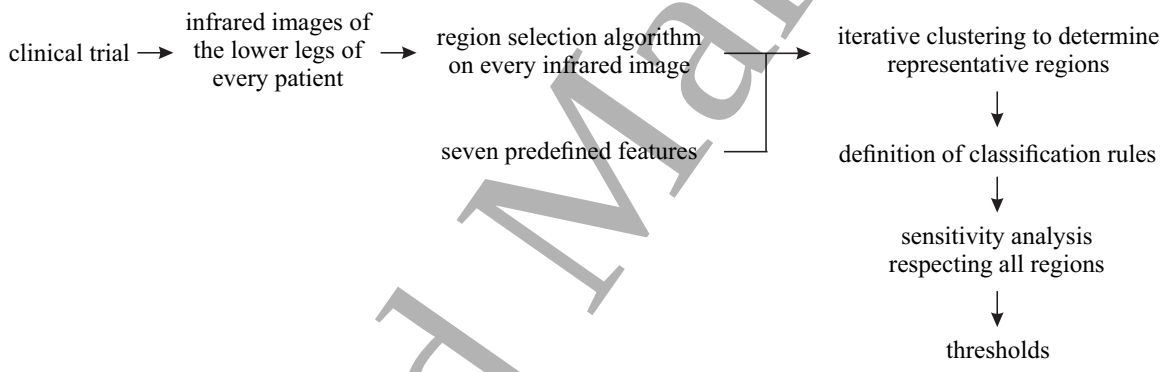

Figure 1. Work flow of the study methodology for the detailed analysis of thermal properties of the lower legs of patients with CVD.

2.1. Clinical trial

The clinical trial was conducted at the Vein Center of the Departments of Dermatology and Vascular Disorders, Ruhr-University Bochum. The trial was approved by the ethics committee of the Medical Department of Ruhr University Bochum under register number 17-6146 and has been registered in the German Clinical Trials Register with registration number DRKS00013886. Over a period of five days, images of the lower legs of 36 patients were recorded. Visual RGB images were captured with a digital camera (Canon EOS 60D, Canon, Tokio, Japan) and infrared images with the VarioCAM HD head 800 (InfraTec GmbH, Dresden, Germany). The visual images serve as a reference in the discussion of this publication; only the infrared images were processed.

The cameras were mounted on a tripod and placed in a treatment room as shown in figure 2. The VarioCAM has a focal plane array size of 1024×768, resulting in infrared images with a spatial resolution of 1024×768 pixels. Its noise equivalent differential temperature (NEDT) is $\delta_C = 30\,\mathrm{mK}$. The infrared sensors capture photons in the

spectral range of 7.5 μm to 14 μm and output the temperature value of each pixel in °C with a measurement uncertainty of ± 1 °C. Room temperature was 22.5 °C on average with a standard deviation of 0.8 °C. The emissivity was estimated to $\epsilon = 0.98$ for all bodies. For image acquisition, the patient stood approximately 60 cm away from the tripod. The lengthwise field of view was approximately 50 cm for all patients, resulting in a spatial resolution of 0.42 mm^2. The images were captured simultaneously with both camera systems after in-depth clinical treatment of the patients, and in case of a florid ulcer, before the new bandage was applied. In case of a CVD without ulcer, both legs were recorded. In case of an ulcer, only those legs where an ulcer was apparent were captured.

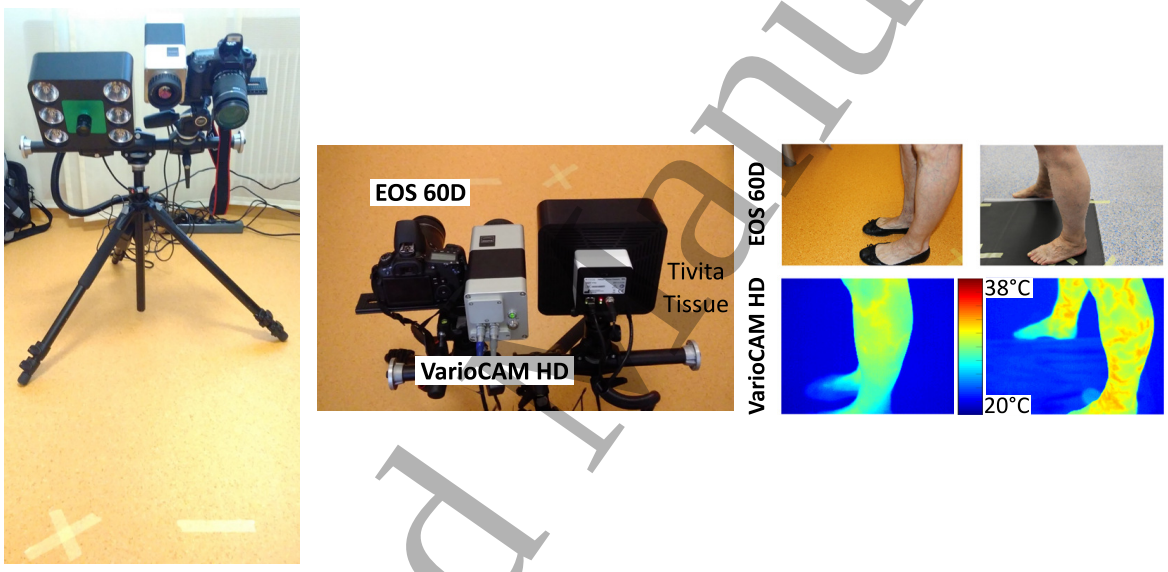

Figure 2. Camera setup and exemplary visual (EOS 60D) and infrared (VarioCAM HD) images conducted at the Center for Venous Disorders of the Department of Dermatology and Vascular Surgery, Ruhr University Bochum. Patients stood approximately 60 cm in front of the tripod on the strip placed on the ground. Images of the lower legs of two patients recorded with the same setup in two different treatment rooms are shown on the right. Note that the TIVITA Tissue System (Diaspective Vision GmbH, Am Salzhaff, Germany) was employed to record additional hyperspectral images. However, these images are not further considered in this publication.

The 36 patients were diagnosed by experienced health professionals. Six patients were not diagnosed with a CVD and classified as noCVD. The remaining patients were classified as CVD but no CVI (C_1 - C_2, 9 patients), CVI but no ulcer (C_3 - C_5, 10 patients), or as florid ulcer (C_6, 11 patients). The patient's age ranged from 29 years to 88 years, averaging 63.5 years for the trial population. Mean age increases with the severity of CVD, patients with C_1 - C_2 averaging 55.8 years, those with florid ulcer averaging 74 years.

2.2. Region selection algorithm

The infrared images were processed with the objective to connect image pixels to regions that are warmer or colder than surrounding tissues, as such temperature differences are expected inside pathological anatomies (Gatt et al. 2015). The two-sided algorithm proposed in this work is built on three sub-algorithms: (a) leg segmentation, (b1) and (b2) seed point detection, and (c1) and (c2) local region growing. The workflow of this region selection algorithm is given with exemplary images in figure 3.

In a first step (a), the leg was segmented from the background of the image using adaptive segmentation. The centers of warm regions were detected modifying an existing morphological top hat filter for the detection of blood vessels in human faces (Buddharaju and Pavlidis 2007) (b1). Cold regions were identified based on increased local temperature variations (LTV) (b2). LTV was computed in °C for all pixels as the local standard deviation

$$LTV = \sqrt{\frac{1}{J}\sum_{j\epsilon A}(T_j - \overline{T})^2}\,, \tag{1}$$

where A are pixels within a radius of 5 mm (complies to 7 pixels in the infrared images) of the pixel, J the number of pixels in A, T_j the temperature of a proximate pixel j, and $\overline{T}$ the mean temperature of A. An LTV of 0.5 °C implies that if two pixels within A are compared, their temperatures differ by 0.5 °C on average. As A considers pixels within 5 mm only, LTV is expected to be close to 0.0 °C in healthy legs, where skin temperature typically changes over larger distances (Gatt et al. 2015). After the identification of warm (b1) and cold (b2) seed points, pixels with similar temperatures were added using region growing for the warm (c1) and cold (c2) regions. A detailed description the algorithms is given in the Appendix.

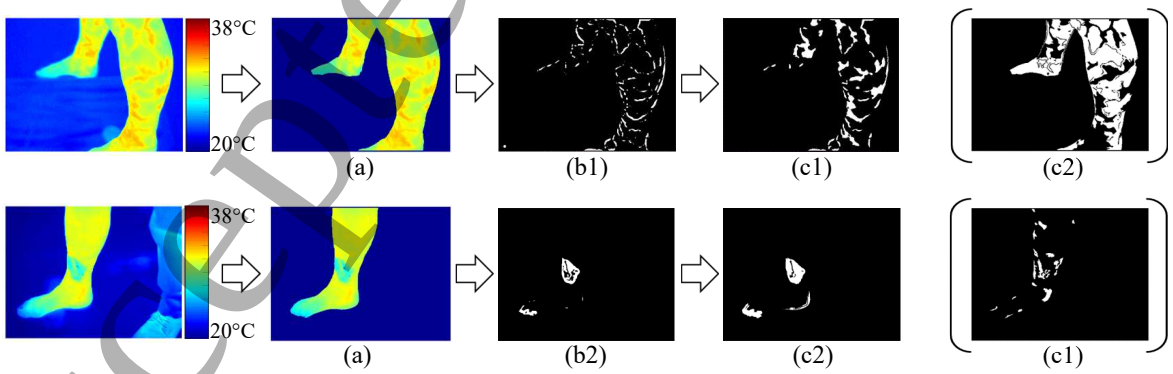

Figure 3. Selection algorithm for the identification of regions with similar thermal properties, exemplified on two infrared images. The top row shows the lower leg of a patient diagnosed with C_3 - C_5 and multiple local increased temperatures. The bottom row shows a patient with C_6 and a region with locally decreased temperatures. (a) leg segmentation, (b1) and (b2) seed point detection of warm and cold regions, respectively, (c1) and (c2) local region growing of the respective seed points. Both algorithms were performed on all infrared images.

The algorithms were applied to all infrared images regardless of their patient class. As the selection is independent of absolute thresholds or temperature values that are found in literature, it is not guaranteed that detected regions correspond to a pathology. This universal approach allows for the unbiased identification of regions and their thermal properties, but necessitates further examination to identify regions – and thus temperature patterns – that stand representative for the different stages of CVD.

2.3. Features of the regions

A comparative examination of the regions was performed based on seven features that were computed for each region: three spatial features that describe its size, eccentricity and convexity, and the four thermal features median temperature, median LTV, difference in median temperature, and difference in median LTV. Thus, the shape of the region, median temperatures, and variations in temperature over a few millimeters (LTV values) and centimeters (differences in temperature values) were considered. These features were predefined out of a variety of information that can be extracted from the regions, as their properties are easily traceable and comparable.

(i) Size S of the region (mm^2):
S can be computed for each region based on its number of pixels $\#P$,

$$S = \left(\frac{fov}{\min(dim)}\right)^2 \cdot \#P, \tag{2}$$

with fov being the estimated field of view of the image (500 mm) and $\min(dim)$ the length of the smaller image dimensions (768 pixels). Large regions form when temperatures only vary slightly; small regions indicate concentrated, local changes in temperature. The conversion of $\#P$ into a surface area in mm^2 was conducted for illustrative purposes only. Potential inaccuracies comparing the sizes of different regions due to distortions and the positioning of the patients were not compensated.

(ii) Eccentricity E (a.u.):
E describes the ratio between the distances of the foci d_{foci} of an ellipse that has the same second-moments as the region and its major axis length l_{axis} (The Math-Works 2021):

$$E = \frac{d_{\mathrm{foci}}}{l_{\mathrm{axis}}}\,. \tag{3}$$

E lies between zero ($d_{\mathrm{foci}} = 0$), as it applies for circles, and one ($d_{\mathrm{foci}} = l_{\mathrm{axis}}$), which corresponds to a line.

(iii) Convexity C (a.u.):
C describes the third spatial feature. It is the ratio between $\#P$ and the number of pixels in the convex hull of the region $\#H$ (The Math-Works 2021):

$$C = \frac{\#P}{\#H}\,. \tag{4}$$

C is smaller for small regions or regions with rough edges than for large regions or regions with smooth edges.

(iv) Median temperature mT (°C), and

(v) median LTV $mLTV$ of the region (°C).

(vi) Difference in median temperatures ΔmT (°C):
ΔmT is the difference between mT and the median temperature mT_{NH} of the neighborhood (NH) surrounding the region,

$$\Delta mT = mT - mT_{\mathrm{NH}}\,. \tag{5}$$

NH is determined by morphological dilation of the region and covers pixels within 30 mm (46 pixels) distance to its edge. This allows for the comparison of temperatures within the same anatomic area.

(vii) Difference in median LTV $\Delta mLTV$ (°C):
$\Delta mLTV$ is the difference between $mLTV$ and the median LTV of the neighborhood $mLTV_{\mathrm{NH}}$,

$$\Delta mLTV = mLTV - mLTV_{\mathrm{NH}}\,. \tag{6}$$

The same NH as for ΔmT is used for the computation of $\Delta mLTV$.

2.4. Data analysis

Data analysis was performed with the aim to derive simple classification rules that relate skin temperature patterns to different stages of CVD. These classification rules originated from an empirical investigation of the features of regions detected in the infrared images. As not all detected regions correspond to a pathology, they were preselected using k-means clustering (Lloyd 1982) before the empirical investigation. This clustering algorithm subdivides feature vectors into a predefined amount of clusters, maximizing the distance between the mean values of the features. For this, all features F of every region were homogenized by normalization

$$nF = \frac{F - \overline{F}}{\mathrm{STD}(F)}\,, \tag{7}$$

with nF being the normalized feature parameter, $\overline{F}$ the mean value of F, and $\mathrm{STD}(F)$ its standard deviation. $\overline{F}$ and $\mathrm{STD}(F)$ were computed based on all regions. The total amount of clusters was set before calculation, affecting the average number of regions that form a single cluster. Here, the amount of clusters was iteratively increased until one cluster coincidentally consisted almost exclusively (to 95 %) of regions of a single class of CVD. As temperature patterns that occur in patients with mild forms of CVD (C_1 - C_2) are expected to also exist in severe forms of CVD, these classes were defined as C_1 - C_6, CVI but no ulcer (C_3 - C_5), or florid ulcer (C_6). The feature values of the regions that compile those single-class clusters were then considered representative of this class. As it is not guaranteed that only one unique cluster exists for each class, the iterative clustering was repeated 1,000 times and a region defined as representative if it occurred in at least 20 % of the clusters. In this study, these settings led to manageable quantities of representative regions of each class.

Analyzing the feature values of these representative regions, threshold-based classification rules (C_1 - C_6, C_3 - C_5, C_6) were determined. The features were compared between each class using two-sided t-tests and most prominent thermal properties empirically selected to derive the classification rules. The thresholds for these rules were set with the aim to maximize the precision of the classification. The final assessment of the patients as the clinically relevant classes noCVD, C_1 - C_2, C_3 - C_5, and C_6 can then achieved by considering the highest-ranking classification rule that was set as true for the respective patient.

3. Results

On average, each of the 64 infrared images was segmented into 19 regions by the region selection algorithm, resulting in a total of 1,199 regions. In the following, the thermal properties of these regions are analyzed in detail to determine common temperature patterns in different classes of CVD.

3.1. Region selection and feature extraction

The feature values of the regions are given for each clinical class in table 1. For analysis, the regions are divided in warm (segmented by algorithms (b1) and (c1)) and cold ((b2) and (c2)) regions. Illustrated are the mean values and standard deviations for each feature.

Table 1. Median values (M) and standard deviation (SD) of the feature values of all regions determined by the region selection algorithm, depicted as M (SD).

Diagnosis	noCVD	C1 - C2	C3 - C5	C6
Regions	196	314	414	275
		warm regions		
S (cm^2)	5 (39)	5 (27)	4 (40)	4 (22)
E (a.u.)	0.90 (0.14)	0.90 (0.13)	0.93 (0.10)	0.90 (0.14)
C (a.u.)	0.78 (0.12)	0.81 (0.14)	0.79 (0.16)	0.77 (0.12)
mT (°C)	31.0 (1.2)	29.5 (1.2)	30.8 (1.7)	30.7 (1.7)
$mLTV$ (°C)	0.05 (0.04)	0.07 (0.04)	0.10 (0.05)	0.08 (0.07)
ΔmT (°C)	0.45 (0.32)	0.57 (0.44)	0.79 (0.59)	0.49 (0.58)
$\Delta mLTV$ (°C)	-0.01 (0.03)	-0.00 (0.04)	-0.01 (0.06)	-0.01 (0.06)
		cold regions		
S (cm^2)	93 (361)	85 (455)	54 (412)	4 (33)
E (a.u.)	0.90 (0.13)	0.88 (0.15)	0.88 (0.12)	0.89 (0.16)
C (a.u.)	0.47 (0.15)	0.58 (0.19)	0.64 (0.19)	0.71 (0.21)
mT (°C)	29.6 (1.4)	28.2 (1.2)	29.7 (2.0)	28.5 (1.6)
$mLTV$ (°C)	0.07 (0.04)	0.06 (0.04)	0.09 (0.11)	0.17 (0.18)
ΔmT (°C)	-0.69 (1.06)	-0.48 (0.96)	-1.13 (1.49)	-1.59 (1.17)
$\Delta mLTV$ (°C)	-0.00 (0.04)	-0.01 (0.04)	-0.02 (0.12)	0.05 (0.18)

The cold regions detected in patients without ulcer have a mean size of 72.8 cm^2. The cold regions of patients with ulcer and all warm regions are comparatively small, with mean sizes of 4 cm^2. The standard deviations of the sizes of both cold and warm regions are large compared their mean values. With an average of −1.59 °C, the absolute temperature difference ΔmT of cold regions in patients with an ulcer is larger than in other classes. Additionally, their intra-regional local temperature variations (LTV) are largest on average with $mLTV = 0.17\,°C$. However, the features have intra-class variations that are wider than the inter-class differences. Therefore, significant differences are not apparent, emphasizing the importance of post-segmentation of the regions.

3.2. Representative regions and classification rules

Of the 1,199 regions, 86 were determined as representative by the iterative clustering algorithm: 40 regions that represent C_1 - C_6, 24 regions C_3 - C_5, and 22 regions C_6. These representative regions repeatedly occur in clusters of the respective patient class. Their feature values are evaluated in figure 4.

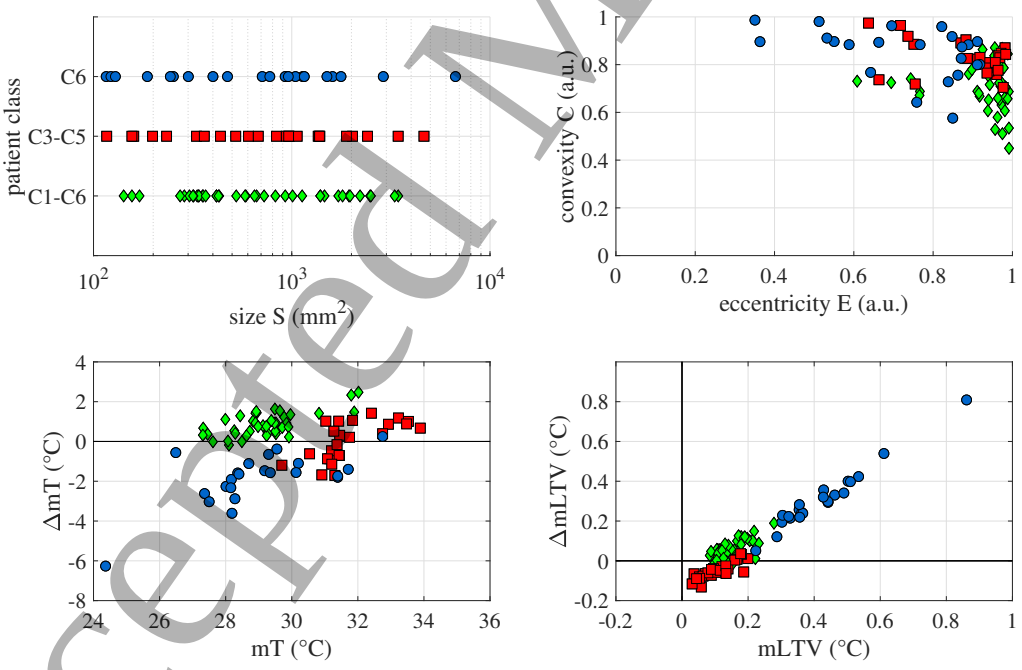

Figure 4. Feature values of the representative regions extracted from the iterative clustering algorithm. 22 blue circles describe regions on legs of patients with ulcer (○ , C_6), 24 red squares of patients with CVI (□, C_3 - C_5), and 40 green diamonds of patients with any form of CVD (♢, C_1 - C_6).

All representative regions are between 1 cm^2 and 10 cm^2 in size and thus small compared to the surface area of an adult lower leg. This means that local patterns were

selected as representative of a stage of CVD rather than large regions of connected skin areas with similar temperatures. Comparing the sizes of the representative regions using two-sided t-tests implies with p-values above 0.5 a significant overlap of this feature for all stages of CVD (table 2). The convexity C is between 0.45 and 0.87 for regions from class C_1 - C_6 and thus lower than for other classes, indicating a low surface-to-circumference ratio. C is similar for C_3 - C_5 and C_6 with a p-value of 0.40. The eccentricity E ranges from 0.6 to 1.0 for C_1 - C_6 and C_3 - C_5 (p-value = 0.08), with values being smaller for C_6. Large eccentricity is generated by linear objects, whereas the regions representing C_6 are more circular. For all classes, convexity decreases with increased eccentricity, as the surface-to-circumference ratio is smaller for linear than for circular objects.

Table 2. Calculated p-values (rounded to two digits) of two-sided t-tests under the null hypothesis that the means of the features of the compared representative regions are equal. S = Size, E = Eccentricity, C = Convexity.

	S	E	C	mT	ΔmT	mLTV	ΔmLTV
C1-C6 v. C3-C5	0.54	0.08	0.00	0.00	0.00	0.00	0.00
C1-C6 v. C6	0.65	0.00	0.00	0.55	0.00	0.00	0.00
C3-C5 v. C6	0.95	0.00	0.40	0.00	0.00	0.00	0.00

The four temperature-based features median temperature mT, difference in median temperature ΔmT, median local temperature variation $mLTV$, and difference in median local temperature variation $\Delta mLTV$ show less overlap between the three classes than the spatial features. Exceptions are mT from class C_1 - C_6 with an average of 29.2 °C and C_6 with an average of 29.5 °C (p-value = 0.55). In addition, regions representing CVD (C_1 - C_6) demonstrate small $mLTV$ and $\Delta mLTV$ values below 0.2 °C. Regarding ΔmT, all C_1 - C_6 regions have positive temperature differences, indicating that regional increases in temperature appear in patients with CVD. Considering the test results in table 2 and figure 4, this relation is identified as the most distinct feature and selected as the classification rule for the assessment of C_1 - C_6. However, by disregarding the other features, the number of false positive classifications inescapably increases. Therefore, sensitivity analysis was performed to define a stringent threshold, maximizing the precision of this rule. The final thresholds and rules that follow from the analysis of the representative regions are given in table 3.

Table 3. Thresholds and rules for the classification of chronic venous diseases.

C1-C6	$\Delta mT > 1.5\,°C$
C3-C5 a)	$mT > 32\,°C$ & $\Delta mT > 1.0\,°C$
C3-C5 b)	$mT > 30\,°C$ & $\Delta mT < -1.0\,°C$
C6	$\Delta mT \cdot mLTV < -0.5\,°C^2$

The regions representing C_3 - C_5 also show minor $mLTV$ and $\Delta mLTV$ values below

0.2 °C. One way to distinguish this patient group is to divide its regions into two subgroups dependent on their mT and ΔmT values: one group is defined by high absolute temperature in combination with increased local temperature (C_3 - C_5 a)), the second group by high absolute temperature in combination with decreased local temperature (C_3 - C_5 b)). The presence of both groups then indicates CVI without florid ulcer. Particularly rule C_3 - C_5 b) is valid only in legs where multiple regions with increased temperatures are apparent, as these regions need to surround a region for it to meet this rule. Regions representing patients with florid ulcer (C_6) consistently show $mLTV$ and $\Delta mLTV$ values larger 0.2 °C. As $mLTV$ highly correlates to $\Delta mLTV$, only the more easily to compute $mLTV$ is considered further. In addition to elevated $mLTV$, the regions have lower temperatures than surrounding tissues. The classification rule is therefore defined as the product of both properties.

The classification rules allow to classify CVD considering the median temperatures mT, temperature differences ΔmT and the median local temperature variations $mLTV$. The rules disregard all spatial features, as temperature rather than form differentiates the classes. It is suggested that CVD leads to local increases in temperatures on the skin surface of lower legs of at least 1.5 °C. This is independent of the absolute temperature. Temperatures exceeding 32.0 °C in an environment where median temperatures are at least 1.0 °C lower in combination with regions warmer than 30.0 °C surrounded by tissues where mean temperatures are at least 1.0 °C higher, are apparent in patients with CVI. Ulcers result in regions that are colder than their surrounding and simultaneously show local temperature variations (LTV). For instance, a region is associated with C_6 if the temperatures inside the region vary by at least $mLTV = 0.5$ °C within 5 mm (see the definition of LTV in section 2.2), while at the same time being at least $\Delta mT = -1.0$ °C colder than the surrounding skin.

3.3. Classification of chronic venous diseases

The eligibility of the classification rules was investigated by applying them to the infrared images of all patients. If none of the regions detected by the region selection algorithm met a classification rule, the respective patient was assessed as noCVD. The infrared images of this group are displayed in figure 5 (a). Each image is captioned by the clinical trial ID of the patient and their diagnosis. The lower legs show no significant local differences in temperature. Patients with partial arterial occlusion disease (paOD) and diabetes mellitus in part exhibit severely increased temperature. This characteristic is, however, evenly distributed over the entire leg. One patient (ID 1) diagnosed as C_1 - C_2 but assessed as noCVD possessed local increases in temperature on both legs. However, these regions were not 1.5 °C warmer than the surrounding skin, therefore not meeting the rule for C_1 - C_6.

If one leg of a patient contained at least one region that met the rule for C_1 - C_6, but no other classification rule, the patient was assessed as C_1 - C_2. The respective infrared images are shown in figure 5 (b). The regions that meet rule C_1 - C_6 are highlighted. If a

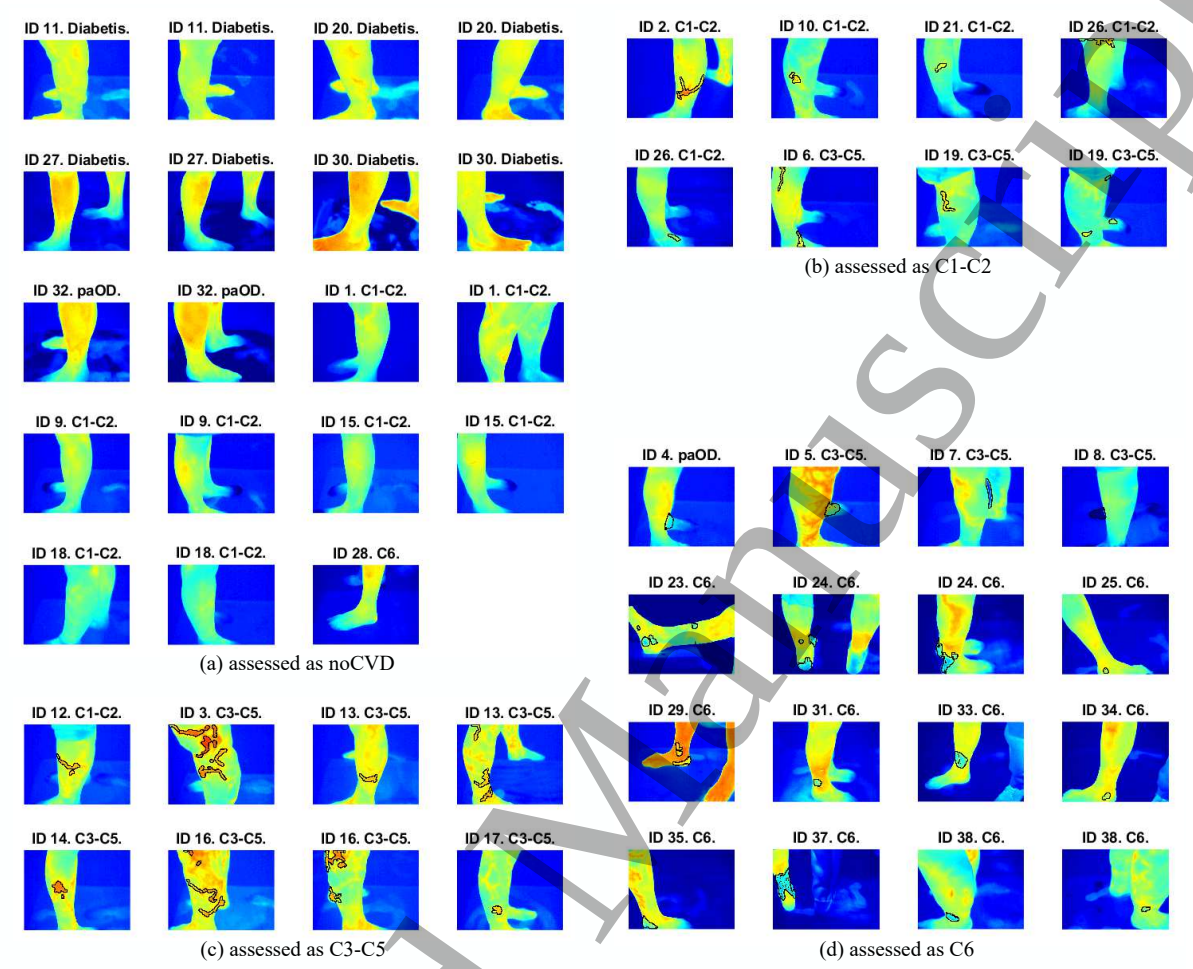

Figure 5. Patients assessed as noCVD (a), C_1 - C_2 (b), C_3 - C_5 (c), and C_6 (d). The assessment is performed applying the region selection algorithm and the threshold-based classification rules to the infrared images. Regions that meet the classification rule for C_1 - C_6, C_3 - C_5 a), or C_6 are highlighted in the respective images (see table 3 for the rules). Each image is captioned by the patient's ID and their clinical diagnosis acting as a ground truth. The color coded infrared images range from 20 °C (dark blue) to 38 °C (bright red).

representative region is apparent in only one leg, the second leg is not shown. The lower legs exhibit single regions with increased temperatures, rather than many regions that meet the rule. These regions are on average 1.97 °C (1.51 °C to 2.91 °C) warmer than the neighboring tissues, with absolute temperatures ranging from 28.93 °C to 33.32 °C (30.87 °C on average).

The infrared images of patients assessed as C_3 - C_5 are given in figure 5 (c). For illustrative purposes, only regions that meet C_3 - C_5 a) are highlighted. These regions have a mean temperature of 32.89 °C (32.02 °C to 34.63 °C) and are on average 1.72 °C (1.01 °C to 2.82 °C) warmer than the neighboring tissues. Therefore, they are 2.0 °C warmer compared to the regions of patients assessed as C_1 - C_2. Furthermore, the number of local regions with increased temperature is more ubiquitous on the leg surface,

even in regions that do not meet the rules. For instance, the lower legs of patient with ID 13 showed – additionally to three regions that meet C_3 - C_5 a) – evenly spaced increases in temperature.

The infrared images of patients assessed as C_6 are given in figure 5 (d). The regions that meet the classification rule are highlighted. Four patients (IDs 4, 5, 7, 8) are assessed as C_6 even though no florid ulcer is apparent. Here, transitions between the front and back leg in the 2D image are not excised by the adaptive segmentation algorithm. These regions show low background temperatures and large LTV at their edges and were thus classified as C_6. This erroneous classification is due to imperfect image acquisition and not poor classification rules, therefore these regions were manually excised. Hiding the erroneous regions, the four patients are classified by the algorithms as noCVD (ID 4), C_3 - C_5 (ID 5), and C_1 - C_2 (IDs 7, 8), respectively. The regions of the remaining images show local decreases in temperature of on average $-2.62\,°C$ ($-6.27\,°C$ to $-1.10\,°C$), and increased LTV of $0.40\,°C$ ($0.19\,°C$ to $0.86\,°C$). These LTV are unique to this patient class, being 4.6 times larger than the average value of all remaining regions (their mean LTV being $0.087\,°C$). In multiple cases (IDs 23, 24, 25, 29, 31, 33, 34, 35, 37, 38), the regions are surrounded by warm areas with low LTV values. Therefore, they stand out within the patient's leg, showing particular temperature patterns rather than fundamental leg properties.

A statistical analysis of the results is given in table 4. Here, the empirically determined classification rules are applied to all patients. Of the 36 patients, 30 were clinically diagnosed with a CVD (C_1 - C_6). 25 patients were classified as C_1 - C_6 using the rules, all being true positive classifications, leading to a precision and a specificity of 100 %. On the other hand, five false negatives occur, resulting in a sensitivity of 83.33 % and a negative predictive value (NPV) of 54.55 %. Identifying a CVI without ulcer (C_3 - C_5) is achieved with a precision of 83.33 %, as only one of the six positive tests is false. The sensitivity is with 50 % comparably low; five of the ten patients diagnosed with C_3 - C_5 are correctly identified. Best test results were achieved classifying patients with ulcer. Ten of the eleven patients with ulcer were detected accordingly. Concurrently, one false negative and zero false positives occur. Therefore, the precision and sensitivity are 100 %. The sensitivity is 90.91 % and the NPV 96.15 %.

4. Discussion

As no ground truth is available for the analysis of regions in infrared images of patients with CVD, selected infrared and visual images are compared in figure 6 to gain further insights on the temperature patterns. The regions classified in the infrared image of a patient with CVI (C_3 - C_5, figure 6 (a)) correspond to visible varicose veins, indicating that temperatures above $32.0\,°C$ occur at varicose veins. This relationship between increased skin temperatures and (varicose) veins has been shown by other research groups in theory (Draper and Boag 1971) and practice (Bagavathiappan et al. 2009, Haeger and Bergman 1963). Martins *et al.* (Martins et al. 2012) further

Table 4. Statistics between the classification using the proposed rules (labeled as *test positive* and *test negative*) neglecting erroneous regions and the clinical diagnosis of all patients for different stages of CVD. NPV = negative predictive value.

Patients with CVD (C1-C6) (as confirmed by clinical diagnosis)			
	positive	negative	
	30	6	
test positive	true positive	false positive	precision
25	25	0	100 %
test negative	false negative	true negative	NPV
11	5	6	54.55 %
	sensitivity	specificity	
	83.33 %	100 %	
Patients with CVI (C3-C5) (as confirmed by clinical diagnosis)			
	positive	negative	
	10	26	
test positive	true positive	false positive	precision
6	5	1	83.33 %
test negative	false negative	true negative	NPV
30	5	25	83.33 %
	sensitivity	specificity	
	50 %	96.15 %	
Patients with ulcer (C6) (as confirmed by clinical diagnosis)			
	positive	negative	
	11	25	
test positive	true positive	false positive	precision
10	10	0	100 %
test negative	false negative	true negative	NPV
26	1	25	96.15 %
	sensitivity	specificity	
	90.91 %	100 %	

demonstrated the potential of infrared images for the localization of varicose veins.

Figure 6 (b) shows images of a patient diagnosed as C_1 - C_2 but assessed as C_3 - C_5. In contrast to the patient in figure 6 (a), no varicose veins are visible in the RGB image. However, the thermal properties closely resemble those found in patients with CVI, potentially identifying a deep varicose vein. In future studies, subsequent duplex sonography could be applied to these regions to search for truncal reflux, and thus to investigate whether the regions are precursors of a worsening of the CVD.

The images of a florid ulcer are given in figure 6 (c). The infrared region matches the edge of the visible wound. These regions on average exhibit reduced temperatures of $-2.6\,°C$ and a LTV of $0.4\,°C$ within the clinical trial, indicating that these patterns occur in florid ulcers. The finding that chronic wounds show reduced temperatures

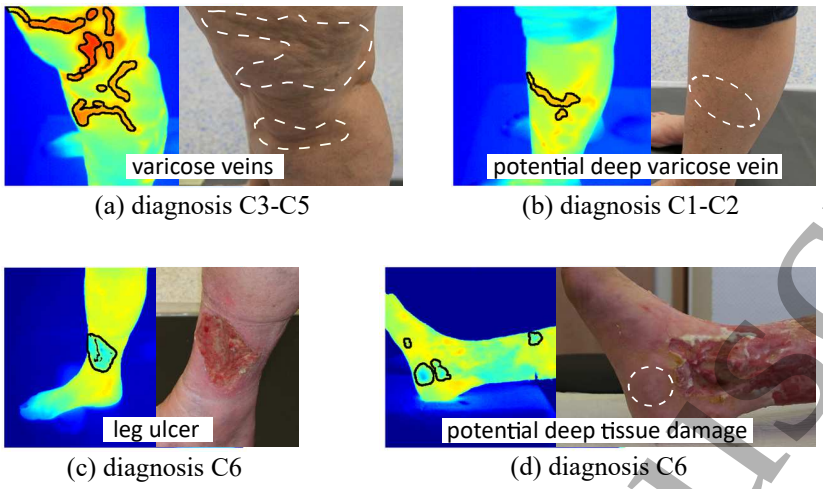

(a) diagnosis C3-C5 (b) diagnosis C1-C2

(c) diagnosis C6 (d) diagnosis C6

Figure 6. Infrared images with highlighted thermal regions and respective RGB images of four patients. The color coded infrared images range from 20 °C (dark blue) to 38 °C (bright red). Sub-figure (a) shows that visible, severe varicose veins correspond to infrared regions. In sub-figure (b), no varicose veins are visible in RGB image, the detected infrared region potentially identifying a deep varicose vein. A florid ulcer corresponds to the representative infrared region in sub-figure (c). One region detected in the infrared image of sub-figure (d) does not correspond to ulceration, potentially detecting deep tissue damage.

agrees with literature (Dini et al. 2015, Gethin et al. 2018, Trandel et al. 1975). LTV values have to our knowledge not been investigated so far. From the presented work we suggest that LTV may indicate pathological tissues. In one patient with extensive ulcer (figure 6 (d)), regions were detected in the infrared image that did not correspond to the visible wound; rather, the temperature properties appear on intact skin. With regard to the findings of Koerner and coworkers (Koerner et al. 2019), deep tissue injuries lying underneath intact skin are visible in infrared images. The region might therefore outline deep tissue injuries, potentially signaling a hidden enlargement of the wound.

Considering the assessment of CVD, one false positive occurred where one patient was falsely classified as CVI (table 4). This patient has been discussed above and visualized in figure 6 (b). As the thresholds of the rules were empirically set to maximize precision, sensitivity and NPV were comparably low for all classifications. Five patients diagnosed with C_1 - C_6 did not show the associated thermal properties. Furthermore, only half of the patients diagnosed with C_3 - C_5 was assessed respectively, resulting in a sensitivity of 50 %. However, the classification of ulcers showed compelling results, with a sensitivity of 90.91 %, NPV of 96.15 %, and a precision and specificity of 100 %. Only the florid ulcer of one patient did not meet its classification rule, as its temperatures not significantly differed from the surrounding tissue (ID 28 in figure 5 (a)). Whether or not this effect corresponds to a healing wound could not be clarified in the conducted trial and should be considered in future studies.

Limitations and outlook

The insights presented in this paper are based on data of six patients without CVD, nine with mild forms of CVD, ten with CVI, and eleven with ulcer. Given this sparse amount of participants, no statistical process for their selection was conducted. Furthermore, relative humidity and solar radiation were not documented, potentially leading to uncertainties in the temperature recordings (Moreira et al. 2017). In some cases, the region of interest was not optimally captured: The recorded legs were not perpendicular to the cameras, and transitions between both legs were later mistaken as wounds by the algorithms. Another limitation of this study is depicted by setting the emissivity to $\epsilon = 0.98$ for all skin and wound tissues. Therefore, our findings need to be further investigated in prospective, elaborated trials.

Temperature patterns were empirically identified by post-processing regions detected by the region selection algorithm. This process is laborious and does not guarantee best outcome. Repeatedly, the algorithm did not prevent the formation of large regions if skin temperatures only slightly changed, resulting in significant deviations in the sizes of the detected regions. Particularly large regions were later filtered out by the clustering and not further considered. Therefore, further development of the region selection algorithm could render post-processing steps unnecessary and improve the determination of the classification rules.

The classification rules were derived from and tested with the same data. However, we believe that the heavily simplified rules condition some degree of generalization. Nevertheless, it is plausible that the thresholds will need to be adjusted with more data. As prospective trials will generate more data, existing texture-based or neural network approaches (Vardasca et al. 2018, Magalhaes et al. 2021) should be applied to further increase the knowledge on temperature patterns of CVD and to adjust the proposed rules. These systems could then be utilized to design monitoring systems that robustly detect pathological regions and classify different stages of CVD.

5. Conclusion

Whereas current research on the thermal properties of pathologies focuses on absolute temperatures, the present work shows that relative changes in temperature on the lower leg within a few centimeters and millimeters are sensitive to various stages of CVD. Particularly LTV in combination with reduced temperatures corresponded to tissue damage in our research, identifying ulcers with a precision of 100 % and a sensitivity of 90.91 %. Florid ulcers showed LTV of on average 0.4 °C within the wound bed in combination with decreased temperatures of on average −2.6 °C. These properties were also apparent on intact skin in one patient, potentially detecting deep tissue damage.

Regional increases of 1.5 °C occurred in mild forms of CVD. The regions of patients with CVI were on average 2.0 °C warmer than those in patients with mild CVD, with temperatures above 32.0 °C and increases in temperature by at least 1.0 °C. These

temperature patterns occurred at the location of varicose veins, potentially identifying deep varicose veins in infrared images.

Infrared thermography has the potential to serve as a complementary tool for the early detection of the pathogenesis of CVD. To achieve this goal, more data needs to be collected in large scale studies considering the described temperature patterns to refine the classification rules, or to translate them into intelligent algorithms. This could improve treatment by identifying varicose veins before they progress into deep tissue damages, or deep tissue damages before they develop into a florid ulcer.

Acknowledgments

This work was supported by the Federal Ministry of Education and Research (BMBF, Germany), Grant 16SV7582.

Appendix

(a) Leg segmentation was performed applying adaptive segmentation on the gradient image G of each infrared image I. G was calculated using the Sobel operators $\mathbf{S}_\mathrm{x}$ and $\mathbf{S}_\mathrm{y}$ (Sobel and Feldman 1968),

$$G = \sqrt{(\mathbf{S}_\mathrm{x} * I)^2 + (\mathbf{S}_\mathrm{y} * I)^2}. \tag{A.1}$$

Under the assumption that skin temperature is greater than room temperature and that the transition between leg and background shows the largest gradients, the leg can be segmented from the background utilizing the adaptive segmentation algorithm given in table A1.

Table A1. Adaptive segmentation algorithm.

while $|m_t - m_{t-1}| > \delta_\mathrm{C}$
  $m_{t-1} = m_t$;
  $L = (G > m_{t-1})$;
  $m_t = 0.5 \cdot \left(\overline{G(L)} + \overline{G(\neg L)}\right)$;
end

Let m_t denote the average between the mean gradient of the segmented $\overline{G(L)}$ and of the non-segmented gradient image $\overline{G(\neg L)}$. The NEDT of the infrared camera δ_C then constitutes the stop criterion of the iterative background segmentation. L is a binary image where all pixels of G that have a value greater than the stored average m_{t-1} between mean gradients are set as true. When the stop criterion is met, the leg is defined as the region framed by L.

(b1) Inside the segmented leg, regions R that exhibit increased temperatures were identified based on an existing morphological top hat (TH) filter for the detection of blood vessels in human faces (Buddharaju and Pavlidis 2007). This algorithm identifies

pixels with the maximum value within a filter mask, detecting the centers of elongated regions. Dependent on the size of the filter mask β_{TH}, narrow or broad structures are highlighted. We recommend Buddharaju and Pavlidis (Buddharaju and Pavlidis 2007) for a detailed description of the TH algorithm. As the widths of the regions of interest in the recorded infrared images were not known a-priori, this algorithm was embedded in an iterative environment that alters β_{TH} with each iteration as illustrated in table A2.

Table A2. Iterative top hat filter algorithm.

while $\#R_t > \#R_{t-1}$
  $\#R_{t-1} = \#R_t$;
  $\beta_{\mathrm{TH}} = \beta_{\mathrm{TH}} + 1$;
  $R_t = (\mathrm{TH}(I, \beta_{\mathrm{TH}}) > \delta_{\mathrm{C}})$;
end

Starting from a minimal filter size of 3 pixels $\times$ 3 pixels, β_{TH} is increased until the number of selected regions $\#R$ does not increase any further. R_t is a binary image where pixels that after TH filtering have values above δ_{C} are set as true. When the iterative algorithm stops, the connected regions within R_t are considered seed points. R_t is shown indexed as (b1) in figure 3 for one patient. The filter mask size that resulted in this particular image is $\beta_{\mathrm{TH}} = 7$ pixels.

(c1) The expansion of the connected regions in R_t was performed with local region growing, where the regions are sorted by their median temperature mT in descending order and consecutively grown, starting with the warmest region. A pixel proximate to a region k is allocated to k if

$$T > \max(T_{k,0}) - \gamma \cdot mLTV_{k,0} \tag{A.2}$$

applies. T is the temperature of the pixel, $\max(T_{k,0})$ is the maximum temperature of the unextended region k, $mLTV_{k,0}$ is its median local temperature variation, and γ an arbitrary integer value that was empirically determined to $\gamma = 6$ for all regions and images. As pixels are added to k, new proximate pixels are considered for allocation. If a pixel is already allocated to a different region, the local region growing of k is reset to the seed pixels and the threshold tightened by reducing γ by one. A region was considered for further analysis if its size is above 1 cm^2 (154 pixels).

(b2) Regions with decreased temperatures were not identified by adopting the TH algorithm. In the lower leg, lowest temperatures occur at its edges. An approach based on the TH filter inevitably detects these regions. Hence, the seed points were determined considering temperature-weighted local temperature variations (LTV),

$$wLTV = (\max(T_I) - T) \cdot LTV. \tag{A.3}$$

The weighted LTV $wLTV$ in $^{\circ}\mathrm{C}^2$ is computed multiplying the difference of the maximum leg temperature $\max(T_{\mathrm{I}})$ with the pixel temperature T by the LTV value LTV of the pixel. Thus, low temperatures combined with large temperature variations

result in a large $wLTV$ value. The pixels that show relatively large $wLTV$ were selected by adaptive segmentation as introduced in table A1, where G was replaced by $wLTV$ and δ_C by δ_C^2.

(c2) Local region growing was performed for each region k identified by (b2) by adding adjacent pixels with a temperature below the mean temperature of k, $\overline{T_k}$,

$$T < \overline{T_k}\,. \tag{A.4}$$

The allocation of pixels to multiple regions is averted by successive region growing. The starting regions are sorted in descending order based on their $wLTV$ value. Once a pixel has been added to a region, it is not available for further allocation.

References

Bagavathiappan, S., Saravanan, T., Philip, J., Jayakumar, T., Raj, B., Karunanithi, R., Panicker, T., Korath, M. P. and Jagadeesan, K. (2009). Infrared thermal imaging for detection of peripheral vascular disorders, *Journal of Medical Physics/Association of Medical Physicists of India* **34**(1): 43.

Bagavathiappan, S., Saravanan, T., Philip, J., Jayakumar, T., Raj, B., Karunanithi, R., Panicker, T. M., Korath, P. and Jagadeesan, K. (2008). Investigation of peripheral vascular disorders using thermal imaging, *The British Journal of Diabetes & Vascular Disease* **8**(2): 102–104.

Buddharaju, P. and Pavlidis, I. (2007). Multispectral face recognition: fusion of visual imagery with physiological information, *Face biometrics for personal identification*, Springer, pp. 91–108.

Dini, V., Salvo, P., Janowska, A., Di Francesco, F., Barbini, A. and Romanelli, M. (2015). Correlation between wound temperature obtained with an infrared camera and clinical wound bed score in venous leg ulcers., *Wounds* **27**(10): 274.

Doerler, M., Reich-Schupke, S., Altmeyer, P. and Stücker, M. (2012). Impact on wound healing and efficacy of various leg ulcer debridement techniques, *Journal der Deutschen Dermatologischen Gesellschaft* **10**(9): 624–631.

Draper, J. and Boag, J. (1971). Skin temperature distributions over veins and tumours, *Physics in Medicine & Biology* **16**(4): 645.

Eklöf, B., Rutherford, R. B., Bergan, J. J., Carpentier, P. H., Gloviczki, P., Kistner, R. L., Meissner, M. H., Moneta, G. L., Myers, K., Padberg, F. T. et al. (2004). Revision of the ceap classification for chronic venous disorders: consensus statement, *Journal of Vascular Surgery* **40**(6): 1248–1252.

Fierheller, M. and Sibbald, R. G. (2010). A clinical investigation into the relationship between increased periwound skin temperature and local wound infection in patients with chronic leg ulcers, *Advances in Skin & Wound care* **23**(8): 369–379.

Gatt, A., Formosa, C., Cassar, K., Camilleri, K. P., De Raffaele, C., Mizzi, A., Azzopardi, C., Mizzi, S., Falzon, O., Cristina, S. et al. (2015). Thermographic patterns of the upper and lower limbs: baseline data, *International Journal of Vascular Medicine* **2015**.

Gethin, G., O'Connor, G. M., Abedin, J., Newell, J., Flynn, L., Watterson, D. and O'Loughlin, A. (2018). Monitoring of ph and temperature of neuropathic diabetic and nondiabetic foot ulcers for 12 weeks: An observational study, *Wound Repair and Regeneration* **26**(2): 251–256.

Haeger, K. H. and Bergman, L. (1963). Skin temperature of normal and varicose legs and some reflections on the etiology of varicose veins, *Angiology* **14**(9): 473–479.

Heyer, K., Herberger, K., Protz, K., Glaeske, G. and Augustin, M. (2016). Epidemiology of chronic wounds in germany: Analysis of statutory health insurance data, *Wound Repair and Regeneration* **24**(2): 434–442.

Koerner, S., Adams, D., Harper, S. L., Black, J. M. and Langemo, D. K. (2019). Use of thermal imaging to identify deep-tissue pressure injury on admission reduces clinical and financial burdens of hospital-acquired pressure injuries, *Advances in Skin & Wound care* **32**(7): 312.

Lloyd, S. (1982). Least squares quantization in pcm, *IEEE Transactions on Information Theory* **28**(2): 129–137.

Magalhaes, C., Mendes, J. and Vardasca, R. (2021). Meta-analysis and systematic review of the application of machine learning classifiers in biomedical applications of infrared thermography, *Applied Sciences* **11**(2): 842.

Martins, M., Ribeiro, L. F. and Cury, J. (2012). Diagnostic evaluation of chronic venous insufficiency cases using thermal imaging, *12th European Congress of Thermology*, Vol. 22, European Association of Thermology and Austrian Society of Thermology, pp. 169–176.

McGuiness, W., Vella, E. and Harrison, D. (2004). Influence of dressing changes on wound temperature, *Journal of Wound Care* **13**(9): 383–385.

Moreira, D. G., Costello, J. T., Brito, C. J., Adamczyk, J. G., Ammer, K., Bach, A. J., Costa, C. M., Eglin, C., Fernandes, A. A., Fernández-Cuevas, I. et al. (2017). Thermographic imaging in sports and exercise medicine: A delphi study and consensus statement on the measurement of human skin temperature, *Journal of Thermal Biology* **69**: 155–162.

National Institute for Health and Care Excellence (2013). Varicose veins: diagnosis and management clinical guideline (CG168). Available at: https://www.nice.org.uk/guidance/cg168 (Accessed 08 January 2021).

Purwins, S., Herberger, K., Debus, E. S., Rustenbach, S. J., Pelzer, P., Rabe, E., Schäfer, E., Stadler, R. and Augustin, M. (2010). Cost-of-illness of chronic leg ulcers in germany, *International Wound Journal* **7**(2): 97–102.

Rabe, E., Pannier-Fischer, F., Bromen, K., Schuldt, K., Stang, A., Poncar, C., Wittenhorst, M., Bock, E., Weber, S. and Jockel, K. (2003). Bonn vein study by the german society of phlebology-epidemiological study to investigate the prevalence and severity of chronic venous disorders in the urban and rural residential populations, *Phlebologie* **32**(1): 1–14.

Robertson, L., Lee, A. J., Gallagher, K., Carmichael, S. J., Evans, C. J., McKinstry, B. H., Fraser, S. C., Allan, P. L., Weller, D., Ruckley, C. V. et al. (2009). Risk factors for chronic ulceration in patients with varicose veins: a case control study, *Journal of Vascular Surgery* **49**(6): 1490–1498.

Sheffield, C. W., Sessler, D. I., Hopf, H. W., Schroeder, M., Moayeri, A., Hunt, T. K. and West, J. M. (1996). Centrally and locally mediated thermoregulatory responses alter subcutaneous oxygen tension, *Wound Repair and Regeneration* **4**(3): 339–345.

Sobel, I. and Feldman, G. (1968). A 3x3 isotropic gradient operator for image processing, *a talk at the Stanford Artificial Project in* pp. 271–272.

Stücker, M., Debus, E. S., Hoffmann, J., Jünger, M., Kröger, K., Mumme, A., Ramelet, A.-A. and Rabe, E. (2016). Consensus statement on the symptom-based treatment of chronic venous diseases, *Journal der Deutschen Dermatologischen Gesellschaft* **14**(6): 575–583.

The Math-Works (2021). Image processing toolbox. Available at: https://mathworks.com/help/images/ref/regionprops.html (Accessed 08 January 2021).

Trandel, R. S., Lewis, D. and Verhonick, P. (1975). Thermographical investigation of decubitus ulcers, *Bull. Prosthet. Res.* **10**(10-24): 137–55.

Vardasca, R., Vaz, L. and Mendes, J. (2018). Classification and decision making of medical infrared thermal images, *Classification in BioApps* pp. 79–104.